



Power Electronic Systems
Laboratory

© 2018 IEEE

Proceedings of the International Telecommunications Energy Conference (INTELEC 2018),
Torino, Italy, October 7-11, 2018

Optimized Modulation of a Four-Port Isolated DC/DC Converter Formed by Integration of Three Dual Active Bridge Converter Stages

J. Böhler,
F. Krismer,
J. W. Kolar

Personal use of this material is permitted. Permission from IEEE must be obtained for all other uses, in any current or future media, including reprinting/republishing this material for advertising or promotional purposes, creating new collective works, for resale or redistribution to servers or lists, or reuse of any copyrighted component of this work in other works.



Eidgenössische Technische Hochschule Zürich
Swiss Federal Institute of Technology Zurich

Optimized Modulation of a Four-Port Isolated DC–DC Converter Formed by Integration of Three Dual Active Bridge Converter Stages

J. Böhler, F. Krismer, T. Sen and J. W. Kolar
Power Electronic Systems Laboratory, ETH Zurich, Switzerland
boehler@lem.ee.ethz.ch

Abstract—Multi-port converters have gained more and more interest in research during recent years, due to the increasing field of possible applications, e.g., DC micro grids, energy distribution in electric vehicles and more electric aircraft, and power supplies for cascaded multi-cell converters. This paper presents an optimized modulation strategy for a bidirectional multi-port DC–DC converter, which consists of the Integration of Three (3) conventional Dual-Active Bridge (I3DAB) converters into a structure that combines the primary-side full bridges into a common three-phase two-level inverter. The resulting structure features one input port and three isolated output ports. By utilizing so far unused degrees of freedom for the control of the power converter, it is shown that a reduction of the power dissipation can be achieved by adapting the primary-side duty cycles to the output power levels. According to the outcome of a comparative evaluation of conventional and optimized modulation strategies for an example system with input and output port voltages of 700 V and 3×100 V, respectively, and with a total nominal power of 3×4 kW, reductions of the conduction losses of up to 23% and reduced additional hardware efforts to achieve ZVS operation (with regard to reduced transformers' magnetizing inductances) within wide power ranges are achievable and are also expected for deviating port voltages. Thus, in combination with the presented optimized modulation strategy, the I3DAB converter is found to be well suited to multi-port applications that require bidirectional conversion capabilities, galvanic isolation, and are subject to unequal load conditions with substantially different power levels provided by the output ports.

I. INTRODUCTION

Bidirectional and isolated multi-port converters are beneficial with respect to efficiency, part count, and system complexity in applications where isolated power conversion between multiple sources and loads is required. Prominent examples are DC micro grids, which gain more and more interest due to the integration of renewable energy sources into the distribution grid, since energy needs to be exchanged between different parts of equipment (energy sources, distributed energy storage components, and loads) [1]. Further applications include power systems installed in electric vehicles (charging infrastructure or energy exchange between different DC-buses) [2,3], the interconnections of several DC systems required in More Electric Aircraft [4], and multi-cell cascaded H-bridge structures where the inverter stage of each converter cell requires its individual isolated DC power supply [5]. Thus, bidirectional multi-port converter topologies are an active research topic since many years, which is confirmed by a large number of related scientific contributions [6]–[8].

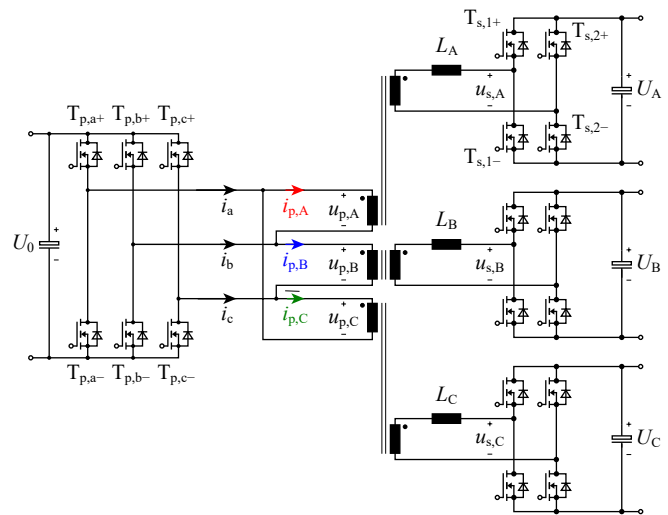


Fig. 1. Converter topology formed by Integration of Three (3) Dual Active Bridge (I3DAB) converter stages.

The considered work investigates a power converter system with four ports, where one main (primary-side) port provides power to three isolated secondary-side ports. A respective conventional realization employs multiple two-port converters, e.g. Dual Active Bridge (DAB) converters, that share a common input DC port. This solution features an independent control of the different converters at the cost of a high number of power semiconductors. A reduction of the required power switches can be achieved by replacing the converters' full bridges by half bridges, which, however, reduces the degrees of freedom for control. Alternatively, multi-port DAB converters realize highly integrated solutions [4,9], respective investigations, however, reveal a comparably high complexity with regard to converter control and optimization. Furthermore, in the considered application, the primary-side full bridge of a multi-port DAB converter is subject to the total power delivered to all output ports. A distribution of the total power to more than two half bridges is achieved by the Integration of Three (3) Dual Active Bridge (I3DAB) converters and leads to the converter topology proposed in [10] and depicted in **Fig. 1**: it uses a three-phase two-level inverter on the primary side, e.g., realized with a conventional six-pack power module and features a reduction of the number of power semiconductors, compared to three parallel operated DAB converters. Besides

the investigations of the I3DAB converter presented in [5,10], a variation of this concept has been recently used to realize a resonant power converter [11]. However, all documented investigations related to the I3DAB converter are confined to the operation with equal power levels and voltages at the output ports. Furthermore, only simplified modulation strategies have been analyzed, which do not utilize all degrees of freedom available for converter optimization.

This paper extends the previously documented results, investigates load scenarios with unequal power levels at the output ports, and presents the development of an optimized modulation strategy, which takes previously unused degrees of freedom for converter control into consideration in order to achieve minimum conduction losses. The structure is organized as follows. **Section II** introduces the operating principle of the I3DAB converter and specifies the modulation parameters available for converter control. **Section III** presents an optimization procedure based on a fundamental frequency analysis of the converter waveforms, which minimizes total conduction losses of the system. Finally, in **Section IV**, the results obtained from the optimization are analyzed and verified by means of numerical circuit simulation and **Section V** concludes this paper.

II. SYSTEM DESCRIPTION

The investigated I3DAB converter, depicted in Fig. 1, uses three High Frequency (HF) transformers, a three-phase two-level inverter on the primary side, and three full bridges on the secondary sides to power the isolated output ports of the three converter phases A, B, and C. The primary-side winding of each HF transformer is connected to the switching nodes of two adjacent phases of the three-phase inverter, which is illustrated in **Fig. 2** for phase A, and, thus, the system of Fig. 1 has strong similarities to the parallel connection of three DAB converters, since the transformers' stray inductances are utilized for power transfer. For this reason, the basic operating principles of the DAB and the I3DAB converters are the same: the primary-side and secondary-side power converters apply alternating voltage waveforms to HF transformer and stray inductance of the corresponding phase, e.g. $u_{p,A}(t)/n_A - u_{s,A}(t)$ to L_A in case of phase A, in order to generate the transformer currents and provide the required output power. **Fig. 3** depicts examples of these voltage and current waveforms and defines the three control variables that are available for phase A, i.e., the duty cycles of $u_{p,A}$ and $u_{s,A}$ and the phase shift between $u_{p,A}$ and $u_{s,A}$,

$$0 \leq D_{p,A} \leq 1, \quad 0 \leq D_{s,A} \leq 1, \quad \text{and} \quad \frac{\pi}{2} \leq \varphi_A \leq \frac{\pi}{2}. \quad (1)$$

Corresponding definitions apply to the duty cycles and phase shifts of phases B and C, however, due to the integration of the three DAB converters' primary-side full bridges into a single three-phase two-level inverter,

$$D_{p,A} + D_{p,B} + D_{p,C} \leq 2, \quad (2)$$

applies.

Detailed analysis reveals that the selection of $D_{p,A} + D_{p,B} + D_{p,C} < 2$ is feasible and extends the parameter space for optimization, however, further improvements are only achievable

for operation with low power levels at two or three output ports and at the cost of increased complexity due to additional boundary conditions. For these reason, the presented analysis is confined to

$$D_{p,A} + D_{p,B} + D_{p,C} = 2. \quad (3)$$

Thus, compared to the operation of three parallel DAB converters, the total degrees of freedom for the control of the three output power levels reduces from nine to eight (two primary-side duty cycles, three secondary-side duty cycles, and three phase shifts). Furthermore, it is not possible to simultaneously operate all phases with primary-side duty cycles greater than $2/3$, because $D_{p,A} > 2/3 \wedge D_{p,B} > 2/3 \wedge D_{p,C} > 2/3$ violates (3).

Fig. 3 presents the principal waveforms obtained with the conventional modulation strategy described in [5], which operates the primary-side inverter with constant duty cycles of $D_{p,\{A,B,C\}} = 2/3$ and, thus, utilizes only six degrees of freedom, i.e., $D_{\{A,B,C\}}$ and $\varphi_{\{A,B,C\}}$. Consequently, a rectangular voltage as shown in Fig. 3 with an active pulse duration of $2/3$ of the switching period is applied to the primary side of each transformer. Based on the findings related to minimization of apparent power and subsequent simplifications, the conventional modulation strategy suggests the secondary-side full bridges to be operated with duty cycles of

$$D_{\{A,B,C\}} = \frac{2}{3} + (2 - \sqrt{2}) \left| \frac{\varphi_{\{A,B,C\}}}{\pi} \right| \quad \forall \quad |\varphi_{\{A,B,C\}}| \leq \frac{\pi}{2}. \quad (4)$$

The respective phase shifts, $\varphi_{\{A,B,C\}}$, are selected in order to provide the required output power levels.

Based on these considerations and the specifications listed in **Tab. I**, the transformers' turns ratios, $n_{\{A,B,C\}}$, and stray inductances, $L_{\{A,B,C\}}$, can be determined. The DAB converter achieves most efficient converter operation if the turns ratio is equal to the ratio of input to output dc voltages [12] and, thus,

$$n_A = n_B = n_C = \frac{700 \text{ V}}{100 \text{ V}} = 7 \quad (5)$$

results. According to Tab. I, the system provides a maximum power of 6.7 kW at all three output ports and, for this reason, all three stray inductances must not exceed

$$L_{\{A,B,C\},\text{max}} = \frac{U_0 U_{\{A,B,C\}}}{9 f_s n_{\{A,B,C\}} P_{\{A,B,C\},\text{max}}} = 3.3 \mu\text{H}. \quad (6)$$

Based on this result and the considerations of an acceptable increase of the reactive power in the HF converter parts at nominal power (4 kW) and practicable sensitivities of the converter's output dc voltages with respect to changing control parameters at low power,

$$L_{\{A,B,C\}} = 80 \% L_{\{A,B,C\},\text{max}} = 2.7 \mu\text{H} \quad (7)$$

has been selected. Margins of 20 % with respect to L_{max} cover eventually arising additional needs due to losses and short-time transient output currents.

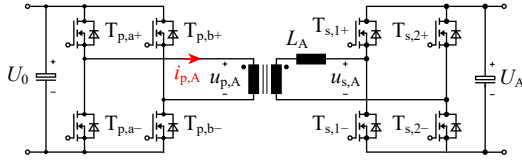


Fig. 2. Phase A of the I3DAB converter. This figure reveals the known topology of a conventional DAB converter.

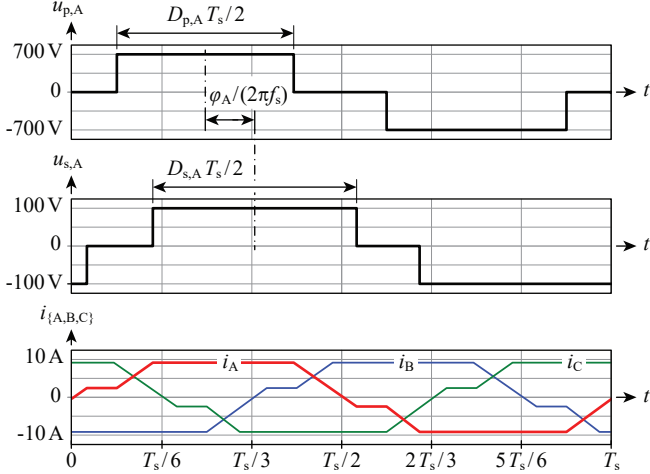


Fig. 3. Voltage and current waveforms for phase A of the I3DAB converter. Since the operating principles of both converter structures is the same, the depicted waveforms show large similarities to the voltages and currents occurring in a standard DAB converter.

TABLE I. SPECIFICATIONS OF THE INVESTIGATED I3DAB CONVERTER.

Nominal dc voltage at input port U_0	700 V
Nominal dc voltages at all output ports, U_A, U_B, U_C	100 V
Rated power at all output ports, $P_{A,0}, P_{B,0}, P_{C,0}$	4 kW
Maximum short-time power, $P_{A,max}, P_{B,max}, P_{C,max}$	6.7 kW
Switching frequency, f_s	50 kHz

III. OPTIMIZATION FOR MINIMUM CONDUCTION LOSSES

This Section describes an optimized modulation strategy, which does not confine $D_{p,\{A,B,C\}}$ to $2/3$, as shown in **Fig. 4**, and, in addition, uses optimized values for $D_{s,\{A,B,C\}}$. The proposed modulation strategy facilitates considerable loss reductions in case of substantially different power levels at the output ports.

A. Developed Modulation Strategy

The presented derivations are based on the Fundamental Frequency Analysis (FFA), to achieve simplified expressions for the output power levels, $P_{\{A,B,C\}}$, and the rms values of the primary-side referred transformer currents, $I_{\{A,B,C\}}$, and still achieve reasonable accuracies [13]. By way of example,

$$I_{A(1)} = \frac{\sqrt{U_{p,A(1)}^2 + n_A^2 U_{s,A(1)}^2 - 2U_{p,A(1)}n_A U_{s,A(1)} \cos(\varphi_A)}}{2\pi f_s n_A^2 L_A}, \quad (8)$$

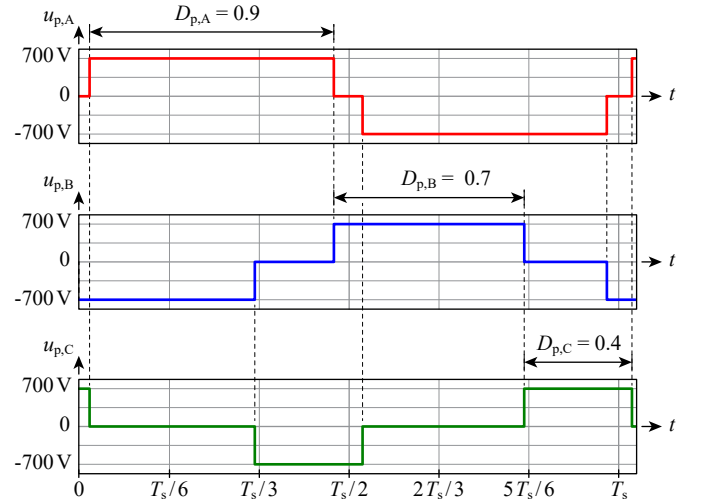


Fig. 4. General voltage waveforms on the primary side for $D_{p,A} = 0.9$, $D_{p,B} = 0.7$, and $D_{p,C} = 0.4$. The dashed lines illustrate the switching instants of the primary-side half bridges.

$$P_{A(1)} = \frac{U_{p,A(1)}U_{s,A(1)} \sin(\varphi_A)}{2\pi f_s n_A L_A}, \quad (9)$$

$$U_{p,A(1)} = U_0 \frac{2\sqrt{2}}{\pi} \sin\left(\frac{\pi}{2} D_{p,A}\right) \quad \forall D_{p,A} \in [0, 1], \text{ and} \quad (10)$$

$$U_{s,A(1)} = U_A \frac{2\sqrt{2}}{\pi} \sin\left(\frac{\pi}{2} D_{s,A}\right) \quad \forall D_{s,A} \in [0, 1] \quad (11)$$

are obtained for phase A, for the fundamental frequency components of $i_A(t)$, the power, $u_{p,A}(t)$, and $u_{s,A}(t)$, cf. Fig. 1, and similar expressions result for phases B and C; the index (1) denotes the fundamental frequency component, $I_{A(1)}$, $U_{p,A(1)}$, and $U_{s,A(1)}$ are rms values.

The conduction losses are calculated with the rms transformer currents $I_{\{A,B,C\}(1)}$ and the equivalent loss resistors, $R_{\{A,B,C\}}$, that are considered in series to the transformers' primary-side terminals. These resistors take the contributions of the on-state channel resistances of the primary-side and secondary-side MOSFETs, $R_{DS,on,p}$ and $R_{DS,on,s,\{A,B,C\}}$,¹ and the primary-side referred effective coil resistances of the HF transformers, $R_{Cu,\{A,B,C\}}$, into account. A two-step derivation, illustrated in **Fig. 5**, yields the contributions of $R_{DS,on,p}$ to the equivalent loss resistances, $R_{\{A,B,C\}}$: in a first step, same conduction losses result if the switches' on-state resistances are moved from the vertical branches of the primary-side half bridges to the connecting wires between the outputs of the half bridges and the HF networks (① in Fig. 5). In a second step, an analytical investigation using wye-delta transformation reveals that the conduction losses remain same for an equivalent resistance of $3R_{DS,on,p}$ being connected in series to each HF transformer (② in Fig. 5).

With regard to the secondary-side full bridges, always two switches conduct the respective transformer current and, thus, the contribution to $R_{\{A,B,C\}}$ is $2n_{\{A,B,C\}}^2 R_{DS,on,s,\{A,B,C\}}$. Based

¹This analysis considers six identical MOSFETs for the primary-side three-phase two-level inverter and four identical MOSFETs for each secondary-side full bridge.

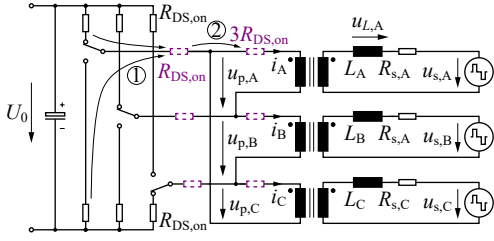


Fig. 5. Illustration of the transformation of the channel on-state resistances of the primary-side MOSFETs, $R_{DS,on}$, into equivalent resistances, $R_{eq,p} = 3R_{DS,on}$, connected in series to the primary-side transformer windings.

on these considerations,

$$R_{\{A,B,C\}} = 3R_{DS,on,p} + R_{Cu,\{A,B,C\}} + 2n_{\{A,B,C\}}^2 R_{DS,on,s,\{A,B,C\}} \quad (12)$$

and the fundamental frequency component of the conduction losses,

$$P_{c(1)} = R_A I_{A(1)}^2 + R_B I_{B(1)}^2 + R_C I_{C(1)}^2, \quad (13)$$

result.

Expression (13) is the basis for the derivation of a modulation strategy that minimizes the conduction losses and enables the calculation of optimal duty cycles, $D_{p,\{A,B,C\},opt}$ and $D_{s,\{A,B,C\},opt}$. In a first step, the secondary-side duty cycles are optimized, since the secondary-side full bridges can be operated independent of each other. In this regard, **Fig. 6** illustrates the conducted calculation and plots the characteristic of $I_{A(1)}^2$ against $D_{s,A}$ for $0 < D_{s,A} \leq 1$ for two different primary-side duty cycles and power levels, i.e., $P_{A(1)} = 1$ kW, $D_{p,A} = 0.4$ in Fig. 6(a) and $P_{A(1)} = 3$ kW, $D_{p,A} = 0.6$ in Fig. 6(b). With respect to the depicted minima of $I_{A(1)}^2$, Figs. 6(a) and (b) reveal optimal duty cycles of $D_{s,A,opt} = 0.42$ and $D_{s,A,opt} = 0.71$, respectively. The corresponding calculation, thus, needs to evaluate

$$\frac{d [I_{k(1)}^2]}{d [\sin(D_{s,k} \frac{\pi}{2})]} = 0, \quad k \in \{A, B, C\}, \quad (14)$$

which yields

$$\sin\left(\frac{\pi}{2} D_{s,k,opt}\right) = \frac{\sqrt{16U_0^4 \sin^4\left(\frac{\pi}{2} D_{p,k}\right) + \pi^6 f_s^2 n_k^4 L_k^2 P_{k(1)}^2}}{4U_0 n_k U_k \sin\left(\frac{\pi}{2} D_{p,k}\right)}. \quad (15)$$

The calculation of optimal primary-side duty cycles involves all converter phases, due to the couplings of the primary-side duty cycles according to (3). For this reason, the complete expression (13) needs to be taken into account. However, due to same ratings of the three output ports, cf. Tab. I, equal equivalent resistances are considered,

$$R_A = R_B = R_C, \quad (16)$$

which simplifies the cost function for the optimization to

$$f_{cost} = I_{A(1)}^2 + I_{B(1)}^2 + I_{C(1)}^2. \quad (17)$$

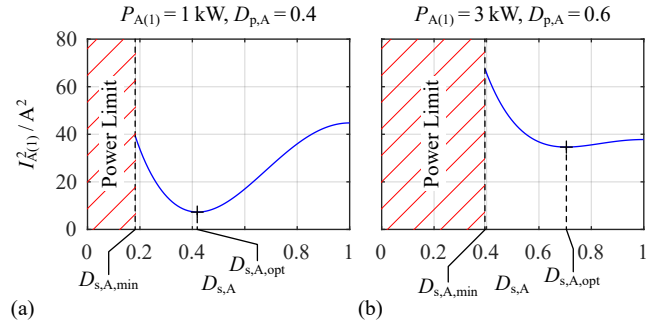


Fig. 6. Squares of the rms values of the primary-side transformer current of phase A for input and output port dc voltages according to Tab. I, $n_A = 7$, $L_A = 2.7 \mu\text{H}$, varying values of $D_{s,A}$, and different power levels and primary-side duty cycles: (a) $P_{A(1)} = 1$ kW, $D_{p,A} = 0.4$, and (b) $P_{A(1)} = 3$ kW, $D_{p,A} = 0.6$. The required output power cannot be provided for $D_{s,A} < D_{s,A,min}$. Minima in $I_{A(1)}^2$ result for: (a) $D_{s,A} = 0.42$ and (b) $D_{s,A} = 0.71$.

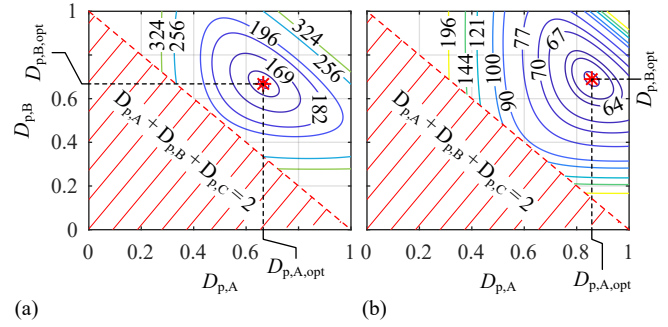


Fig. 7. Results determined for f_{cost} , cf. (17), for input and output voltages according to Tab. I, $n_{\{A,B,C\}} = 7$, $L_{\{A,B,C\}} = 2.7 \mu\text{H}$, different primary-side duty cycles, $D_{p,A}$ and $D_{p,B}$ ($D_{p,C} = 2 - D_{p,A} - D_{p,B}$), optimal duty cycle values for the secondary-side full bridges, and different output power levels: (a) $P_{A(1)} = P_{B(1)} = P_{C(1)} = 4$ kW, (b) $P_{A(1)} = 4$ kW, $P_{B(1)} = 2$ kW, $P_{C(1)} = 1$ kW. Optimal primary-side duty cycles of $D_{p,A} = D_{p,B} = D_{p,C} = 0.67$ and $D_{p,A} = 0.86$, $D_{p,B} = 0.69$, $D_{p,C} = 0.45$ result for the two load scenarios, respectively. Operation in the hatched region is not possible because this would imply $D_{p,C} > 1$ according to (3).

Fig. 7 illustrates the results computed for f_{cost} for $0 \leq D_{p,A} \leq 1$, $0 \leq D_{p,B} \leq 1$, optimized secondary-side duty cycles, and for two different load scenarios: a symmetrical load case with $P_{A(1)} = P_{B(1)} = P_{C(1)} = 4$ kW in Fig. 7(a) and an asymmetrical load scenario in Fig. 7(b) with $P_{A(1)} = 4$ kW, $P_{B(1)} = 2$ kW, $P_{C(1)} = 1$ kW. The hatched area in Fig. 7 denotes combinations of unallowed values for $D_{p,A}$ and $D_{p,B}$, which would violate (3). Due to the operation with different power levels at the output ports, the optimal primary-side duty cycles that minimize the cost function in Fig. 7(b) are $D_{p,A,opt} = 0.86$, $D_{p,B,opt} = 0.69$ and $D_{p,C,opt} = 0.45$, i.e., different to $2/3$ whereas optimal operation in the symmetrical case is achieved for $D_{p,A,opt} = D_{p,B,opt} = D_{p,C,opt} = 2/3$.

The mathematical description of the optimization illustrated in Fig. 7 is

$$\frac{df_{cost}}{d [\sin(D_{p,A} \frac{\pi}{2})]} = 0 \wedge \frac{df_{cost}}{d [\sin(D_{p,B} \frac{\pi}{2})]} = 0. \quad (18)$$

However, no closed-form analytical solution has been found

for (18). Hence, a numerical solver is used to determine the optimal duty cycle values.

With known duty cycles and output power levels, the corresponding phase shifts, $\varphi_{\{A,B,C\},\text{opt}}$, are determined according to (9), which, for phase k , $k \in \{A, B, C\}$, is

$$\varphi_{k,\text{opt}} = \arcsin \left[\frac{\pi^3 f_s n_k L_k P_{k(1)}}{4U_0 U_k \sin\left(\frac{\pi}{2} D_{p,k,\text{opt}}\right) \sin\left(\frac{\pi}{2} D_{s,k,\text{opt}}\right)} \right]. \quad (19)$$

B. Discussion and ZVS

This Section evaluates the optimized modulation strategy for the I3DAB converter specified and designed in Section II and for 24 characteristic operating points that result from the combinations of the selected output power levels listed below.

$$\begin{aligned} P_{A(1)} &= 4.0 \text{ kW} \\ P_{B(1)} &= [0.0, 2.0, 4.0] \times 1 \text{ kW} \\ P_{C(1)} &= [0.0, 0.1, 0.25, 0.5, 1.0, 2.0, 3.0, 4.0] \times 1 \text{ kW} \end{aligned} \quad (20)$$

To begin with, **Fig. 8** depicts the control variables, $D_{p,\{A,B,C\}}$, $D_{s,\{A,B,C\}}$, and $\varphi_{\{A,B,C\}}$, for the conventional modulation strategy presented in [10], which uses $D_{p,\{A,B,C\}} = 2/3$ for all operating points and confines the ranges for $D_{s,\{A,B,C\}}$ to values between $2/3$ and 1, according to (4). With $D_{p,\{A,B,C\}} = 2/3$, the conventional modulation strategy facilitates decoupled control of output power and port voltage of each phase, however, excludes a great range of potential options for improved converter operation. **Fig. 9** presents the control variables determined with the developed optimized modulation strategy and reveals the expected change of the primary-side duty cycles for changing output power levels. The major findings drawn from Fig. 9 are summarized below.

- An increase of the output power of a certain converter phase leads to an increase of the corresponding primary-side duty cycle, e.g., $D_{p,C}$ for increasing $P_{C(1)}$ in Fig. 9, and, due to (3), a decrease of one or both of the remaining primary-side duty cycles.
- The primary-side duty cycles are distributed according to the corresponding power levels, i.e., the greatest primary-side duty cycle results for the converter phase with the highest output power and the smallest duty cycle for the phase with the lowest output power.
- In comparison to the conventional modulation strategy, the linear relationship between $D_{s,\{A,B,C\}}$ and $\varphi_{s,\{A,B,C\}}$ does not apply anymore and the full range of $0 \leq D_{s,\{A,B,C\}} \leq 1$ is utilized.

The optimized modulation strategy achieves a reduction of the value of the cost function by up to 23%, which is detailed in the course of the verification presented in Section IV. However, both, the conventional and the optimized modulation strategies are found to lose ZVS at the primary side at operating points with substantially different power levels of the three converter ports, e.g., one half bridge of the three-phase inverter loses ZVS for $P_{A(1)} = 3 \text{ kW}$, $P_{B(1)} = 3 \text{ kW}$, and $P_{C(1)} = 1 \text{ kW}$. Reduced magnetizing inductances of the

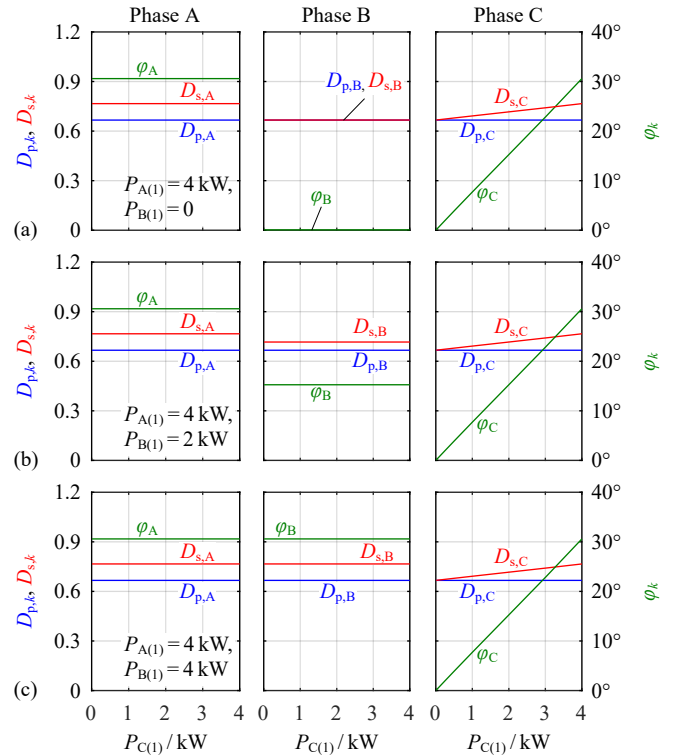


Fig. 8. Control parameters calculated with the conventional modulation scheme proposed in [10] for $P_{A(1)} = 4 \text{ kW}$, $0 < P_{C(1)} < 4 \text{ kW}$, and different power at the output port of phase B: (a) $P_{B(1)} = 0$, (b) $P_{B(1)} = 2 \text{ kW}$, (c) $P_{B(1)} = 4 \text{ kW}$. All primary-side duty cycles are fixed to $D_{p,\{A,B,C\}} = 2/3$. The values of $D_{s,\{A,B,C\}}$ and $\varphi_{\{A,B,C\}}$ are determined by the according power flow, where a linear relationship between $D_{s,\{A,B,C\}}$ and $\varphi_{\{A,B,C\}}$ according to (4) is considered.

HF transformers can be utilized to gain ZVS again and the value of the required magnetizing inductance is used as a Figure of Merit for evaluating the modulation strategies with regard to their suitability for operation with ZVS, i.e., a larger allowable magnetizing inductance denotes a modulation strategy that is more suitable with respect to ZVS. The calculation of maximum allowable magnetizing inductances for 512 different operating points, created from all combinations of $P_{\{A,B,C\}(1)} = [0.0, 0.1, 0.25, 0.5, 1.0, 2.0, 3.0, 4.0] \times 1 \text{ kW}$, returns maximum magnetizing inductances of

$$\begin{aligned} L_{\text{mag,conv}} &< 1.47 \text{ mH} \text{ and} \\ L_{\text{mag,opt}} &< 4.59 \text{ mH} \end{aligned} \quad (21)$$

for the three HF transformers and the conventional and optimized modulation strategies, respectively.² According to this result, the optimized modulation strategy is far more robust with respect to ZVS operation than the conventional modulation.

On a final note, it is worth to mention that both investigated modulation strategies feature complete four-port operation, i.e., bidirectional operation of the three converter phases

² $L_{\text{mag,conv}}$ and $L_{\text{mag,opt}}$ are determined based on the assumption that zero instantaneous current enables ZVS. However, a practical implementation of ZVS requires increased currents at the switching instants. Thus, the magnetizing inductances need to be reduced, accordingly.

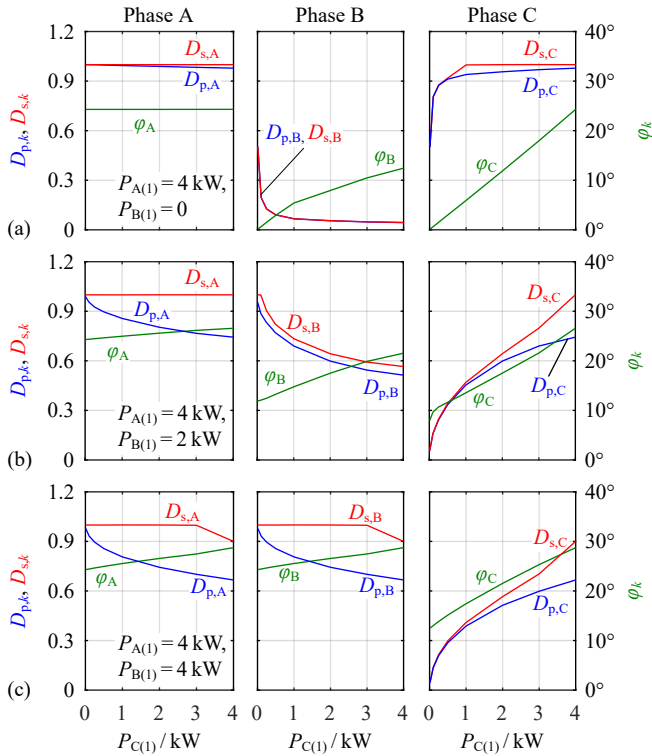


Fig. 9. Control parameters for minimum total rms transformer current, $P_{A(1)} = 4$ kW, $0 < P_{C(1)} < 4$ kW, and different power at the output port of phase B: (a) $P_{B(1)} = 0$, (b) $P_{B(1)} = 2$ kW, (c) $P_{B(1)} = 4$ kW. The primary-side duty cycles are distributed according to the corresponding power levels where increasing power levels correspond with increasing duty cycles of the according phase.

and converter operation with different output port voltages, which is only limited by the maximum output power levels, the requirement of positive port voltages, and the additional limitations imposed by the converter hardware (e.g. thermal limitations).

IV. VERIFICATION AND RESULTS

The results obtained from the optimization described in Section III are verified by means of numerical circuit simulation. For this purpose, two characteristic load scenarios with different output power levels are chosen:

- Scenario I: $P_{A(1)} = 4$ kW, $P_{B(1)} = P_{C(1)} = 0$;
- Scenario II: $P_{A(1)} = 4$ kW, $P_{B(1)} = 2$ kW, $P_{C(1)} = 0.1$ kW.

Fig. 10 and **Fig. 11** depict the simulated waveforms corresponding to the two load scenarios, respectively, and for conventional and optimized modulation strategies. Comparing the primary-side voltage waveforms for both modulation strategies it is clearly visible that for the optimized modulation strategy the active duty cycles applied to the primary sides of the transformers deviate between the phases. In the first load scenario, depicted in Fig. 10, the primary-side duty cycle of the only port delivering output power (phase A) is set to the maximum value of 1. Due to the larger voltage time area applied to the

transformer, the corresponding phase current amplitude can be reduced when compared to the conventional modulation. By reason of (3), the remaining phases are operated with a primary-side duty cycle of $D_{p,B} = D_{p,C} = 0.5$. Power flow for all phases is controlled via their corresponding secondary-side duty cycles and the phase shifts between primary and secondary sides, which are chosen according to (15) and (19).

In the second load scenario, depicted in Fig. 11, the rms currents of phases A and B are reduced by maximizing the primary-side duty cycles of the corresponding phase voltages, which is similar to the results obtained for scenario I, cf. Fig. 10. As a consequence, this leads to a reduction of $D_{p,C}$, resulting in a small active on-time of phase C as the according output power approaches zero. The optimized primary-side duty cycles, thus, allow for low losses in phase C and, at the same time, feature $D_{p,A} \approx 1$ and $D_{p,B} \approx 1$, which enables a reduction of the rms currents in the remaining phases. The optimized modulation strategy reduces the values of the cost function, f_{cost} , defined with (17), from 56 A^2 and 70 A^2 to 40 A^2 and 49 A^2 for load scenarios I and II, respectively.

Fig. 12 presents the values of f_{cost} for both modulation strategies and for the 24 operating points defined with (20), cf. Section III-B. The value of f_{cost} is proportional to the total conduction losses of the converter system and is, thus, a suitable measure for comparison. From the presented graphs it becomes evident that calculated and simulated values of fundamental frequency components exactly match. Compared to the conventional modulation scheme, the optimized modulation strategy achieves reductions of the total conduction losses of up to 23% (e.g., at $P_{A(1)} = 4$ kW, $P_{B(1)} = 4$ kW, and $P_{C(1)} = 0$). As expected, the optimized control of the primary-side voltages is especially favorable for cases where large deviations between the three output power levels occur.

The results of Fig. 12, however, only take the fundamental frequency components into consideration and neglect higher order harmonics in the waveforms. The additional contributions of higher order harmonics increase the power levels and the rms currents in all converter components. In order to compensate the deviations and precisely meet the desired output power levels, the values of $P_{A(1)}$, $P_{B(1)}$, and $P_{C(1)}$, which denote the input parameters for the computation of duty cycles and phase angles, are slightly reduced. Fig. 13 presents the corresponding results, which include all frequency components in rms currents and power levels. The obtained results confirm the effectiveness of the optimized modulation scheme also when taking higher order harmonic components into account, with the conduction losses being reduced by up to 30% (e.g., at $P_A = 4$ kW, $P_B = 4$ kW, and $P_C = 0$). A direct comparison of Figs. 12 and 13 reveals only minor differences between the results obtained with FFA and the detailed results that include all harmonic components, which justifies the presented optimization procedure.

V. CONCLUSION

This paper presents an optimized modulation strategy for the 13DAB converter topology, which minimizes the conduction losses generated by the power converter system. Based on fundamental frequency analysis, the operating behavior of

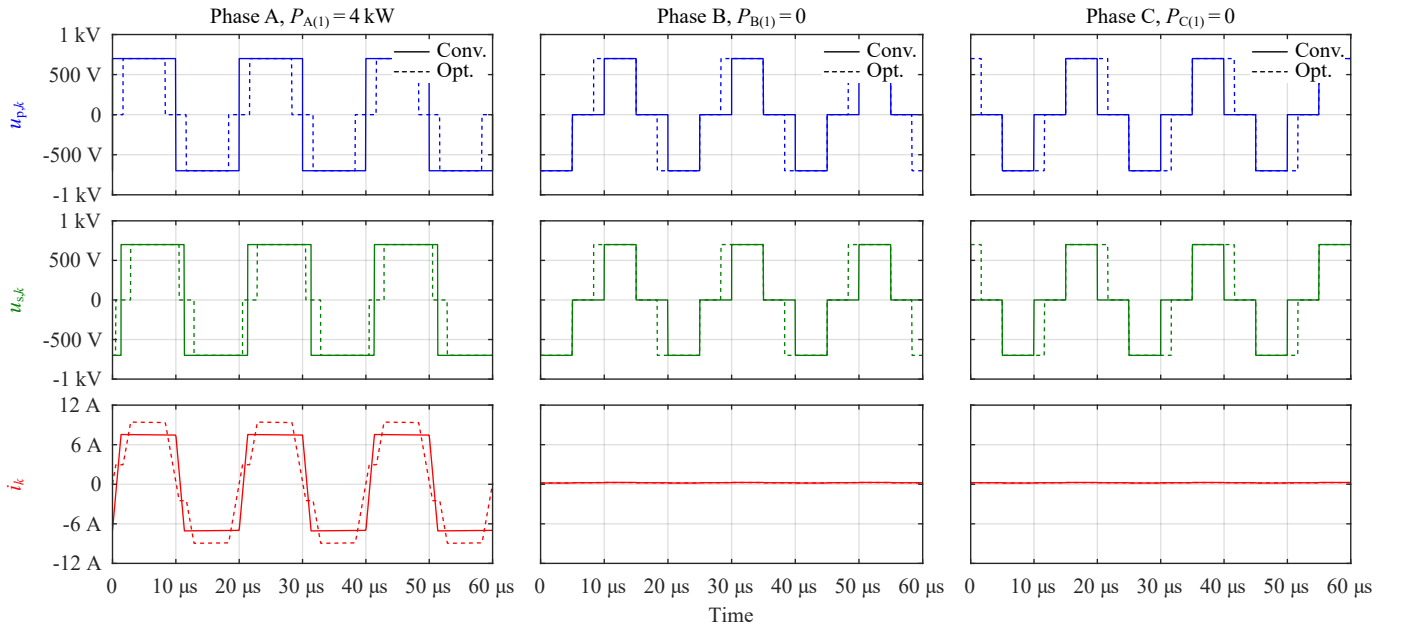


Fig. 10. Simulated voltage and current waveforms for $P_{A(1)} = 4 \text{ kW}$, $P_{B(1)} = 0$, and $P_{C(1)} = 0$. Only one port (phase A) delivers output power, therefore, the according primary-side duty cycle is set to the maximum value in order to minimize the rms current. Due to additional harmonic components which are neglected in the FFA, higher output powers than expected result, leading to total output power levels of $P_A = 4.4 \text{ kW}$ and $P_B = P_C = 0$. The values of the cost function, cf. (17), are 56 A^2 and 40 A^2 for conventional and optimized modulation strategies, respectively.

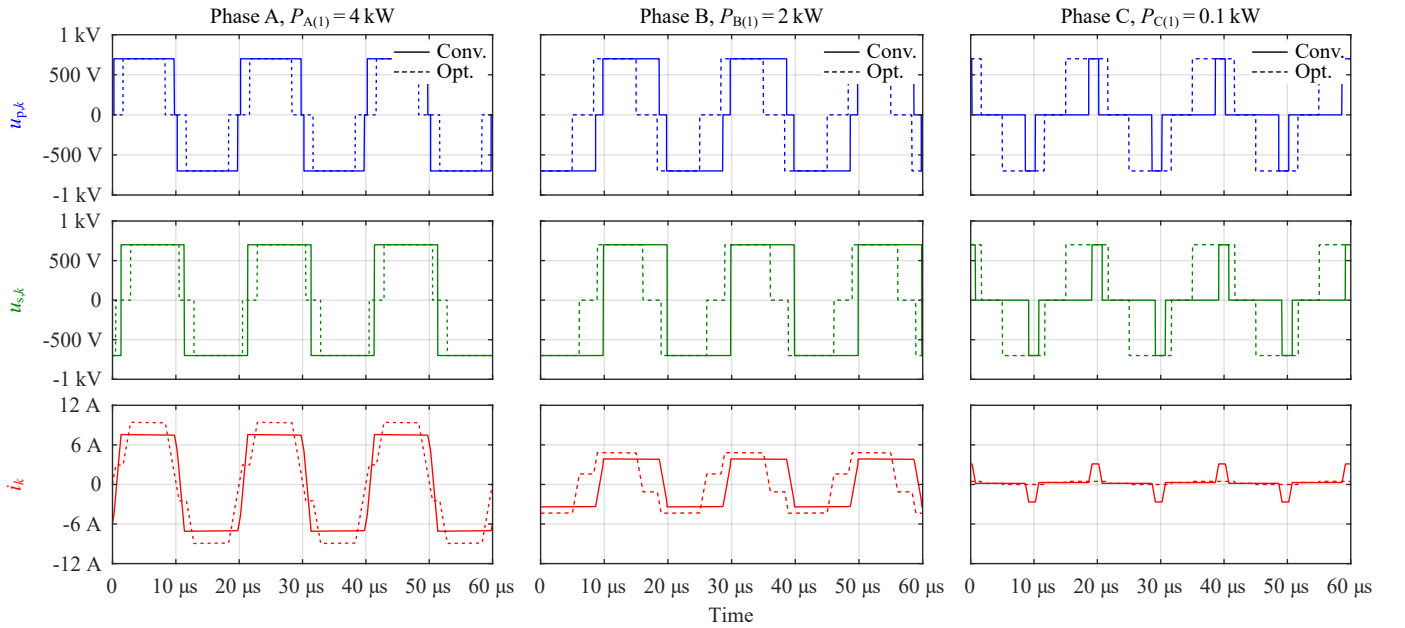


Fig. 11. Simulated voltage and current waveforms for $P_{A(1)} = 4 \text{ kW}$, $P_{B(1)} = 2 \text{ kW}$ and $P_{C(1)} = 0.1 \text{ kW}$. Due to additional harmonic components, increased output power levels of $P_A = 4.4 \text{ kW}$, $P_B = 2.2 \text{ kW}$, and $P_C = 0.3 \text{ kW}$ result. Similar to the results of Fig. 10, increased primary-side duty cycles are used for the phases that are subject to high loads (phases B and C). The values of the cost function, cf. (17), are 70 A^2 and 49 A^2 for conventional and optimized modulation strategies, respectively.

the converter is described and available degrees of freedom for converter optimization are identified. The investigated modulation strategy adapts the primary-side duty cycles in accordance to the output power levels, to achieve reduced rms currents in the power semiconductors and the windings of the HF

transformers. Compared to the conventional modulation strategy, it is found that reductions of the total conduction losses are especially feasible if the output power levels provided by the different output ports are subject to large differences. Furthermore, investigations with respect to ZVS reveal that

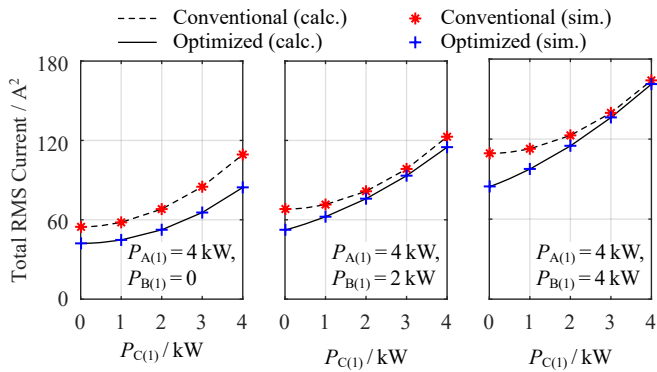


Fig. 12. Comparison of the calculated and simulated rms transformer currents for both modulation strategies. Only the fundamental frequency components of current and power are considered. The simulated results precisely match the calculated values obtained from the optimization. Based on these results, reductions of the conduction losses by up to 23 % are estimated (e.g., at $P_{A(1)} = 4 \text{ kW}$, $P_{B(1)} = 4 \text{ kW}$, and $P_{C(1)} = 0$).

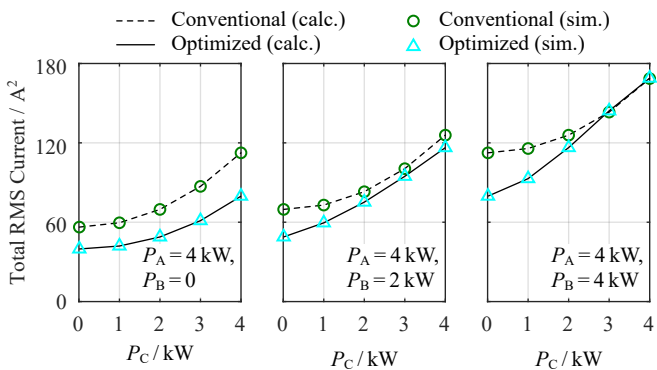


Fig. 13. Simulation results for the conventional and the optimized modulation scheme with all spectral components being taken into account. The simulation results prove that the predicted reduction in conduction losses is still achieved when higher order harmonic components are considered, thereby justifying the presented FFA-based optimization. The optimized modulation strategy reduces conduction losses by up to 30 % (e.g., at $P_A = 4 \text{ kW}$, $P_B = 4 \text{ kW}$, and $P_C = 0$).

the I3DAB converter may lose ZVS in case of unequal load conditions for both, conventional and optimized modulation strategies. However, ZVS can be regained by reducing the magnetizing inductance of the HF transformers.

An exemplary I3DAB converter system serves for the purpose of evaluation. It provides input and output port dc voltages of 700 V and 100 V, respectively, and power levels of up to 4 kW at each output port, i.e., a total power of 12 kW. Depending on the considered operating point, the optimized modulation strategy is found to enable reductions of the total conduction losses of up to 23 %, which is successfully verified by means of numerical circuit simulations. With regard to ZVS, calculated results for 512 different operating points render the optimized modulation scheme more advantageous with respect to ZVS robustness, due to a significantly higher allowable value of the magnetizing inductance (4.59 mH instead of 1.47 mH). Follow-up investigations, in addition, reveal that the optimized modulation strategy achieves reduced losses also in case of deviating port voltages. Currently, the realization of

the hardware prototype is ongoing, which, in a next step, will serve for experimental verification.

According to the obtained findings, the I3DAB converter features a high level of integration combined with the capability to optimize the utilization of its power components with respect to the distributions of the output power levels. Thus, it is highly suitable for multi-port applications, which require bidirectional conversion capability, galvanic isolation, and are subject to unequal load conditions.

REFERENCES

- [1] Z. Wang, "Interleaved multi-phase isolated bidirectional DC-DC converter and its extension," Ph.D. dissertation, Florida State University, March 2012.
- [2] M. Jafari, Z. Malekjamshidi, G. Platt, J. G. Zhu, and D. G. Dorrell, "A multi-port converter based renewable energy system for residential consumers of smart grid," in *Proc. 41st Annual IEEE Industrial Electronics Society Conf. (IECON)*, Yokohama, Japan, 9–12 Nov. 2015, pp. 5168–5173.
- [3] G. Waltrich, J. L. Duarte, and M. A. M. Hendrix, "Multiport converters for fast chargers of electrical vehicles - focus on high-frequency coaxial transformers," in *Proc. IEEE Energy Conversion Congr. and Expo. (ECCE Asia)*, Sapporo, Japan, 21–24 June 2010, pp. 3151–3157.
- [4] G. Buticchi, L. F. Costa, D. Barater, M. Liserre, and E. Dominguez, "A quadruple active bridge converter for the storage integration on the more electric aircraft," *IEEE Trans. Power Electron.*, vol. 33, no. 8, pp. 8174–8186, Sept. 2018.
- [5] H. Wrede, "Beiträge zur Erhöhung von Versorgungssicherheit und Spannungsqualität in der Übertragung und Verteilung elektrischer Energie durch leistungselektronische Betriebsmittel (in German)," Ph.D. dissertation, Ruhr University Bochum, Jan. 2004.
- [6] B. J. D. Vermulst, J. L. Duarte, E. A. Lomonova, and K. G. E. Wijnands, "Scalable multi-port active-bridge converters: Modelling and optimised control," *IET Power Electronics*, vol. 10, no. 1, pp. 80–91, Jan. 2017.
- [7] F. Jauch and J. Biela, "An innovative bidirectional isolated multi-port converter with multi-phase AC ports and DC ports," in *Proc. 15th European Conf. on Power Electronics and Applications (EPE)*, Lille, France, 2–6 Sept. 2013, pp. 1–7.
- [8] J. Schäfer, D. Bortis, and J. W. Kolar, "Multi-port multi-cell DC/DC converter topology for electric vehicle's power distribution networks," in *Proc. 18th IEEE Workshop on Control and Modeling for Power Electronics (COMPEL)*, Stanford, CA, USA, 9–12 July 2017, pp. 1–9.
- [9] L. Costa, G. Buticchi, and M. Liserre, "Optimum design of a multiple-active-bridge dc-dc converter for smart transformer," *IEEE Trans. Power Electron.*, pp. 1–11, Jan. 2018, early access.
- [10] H. Wrede, V. Staudt, and A. Steimel, "A soft-switched dual active bridge 3dc-to-1dc converter employed in a high-voltage electronic power transformer," in *Proc. 10th European Conf. on Power Electronics and Applications (EPE)*, Toulouse, France, 2–4 Sept. 2003, pp. 1–8.
- [11] B. Li, Q. Li, and F. Lee, "A WBG based three phase 12.5 kW 500 kHz CLLC resonant converter with integrated PCB winding transformer," in *Proc. IEEE Applied Power Electronics Conf. and Expo. (APEC)*, San Antonio, TX, USA, 4–8 March 2018, pp. 469–475.
- [12] F. Krömer and J. Kolar, "Efficiency-optimized high-current dual active bridge converter for automotive applications," *IEEE Trans. Ind. Electron.*, vol. 59, no. 7, pp. 2745–2760, July 2012.
- [13] B. Zhao, Q. Song, W. Liu, G. Liu, and Y. Zhao, "Universal high-frequency-link characterization and practical fundamental-optimal strategy for dual-active-bridge dc-dc converter under pwm plus phase-shift control," *IEEE Trans. Power Electron.*, vol. 30, no. 12, pp. 6488–6494, Dec. 2015.